Journal of Computational Physics 228 (2009) 3072–3083

Contents lists available at ScienceDirect

Journal of Computational Physics

journal homepage: www.elsevier.com/locate/jcp

Second-order time evolution of P_N equations for radiation transport

Gordon L. Olson *

Computer and Computational Sciences Division (CCS-2), Los Alamos National Laboratory, 5 Foxglove Circle, Madison, WI 53717, USA

ARTICLE INFO

Article history:
Received 12 June 2008
Received in revised form 9 January 2009
Accepted 12 January 2009
Available online 23 January 2009

Keywords:
Radiation transport
P_N method
Second order
Radiation diffusion
Flux-limited diffusion

ABSTRACT

Using polynomials to represent the angular variation of the radiation intensity is usually referred to as the P_N or spherical harmonics method. For infinite order, the representation is an exact solution of the radiation transport solution. For finite N, in some physical situations there are oscillations in the solution that can make the radiation energy density be negative. For small N, the oscillations may be large enough to force the material temperature to numerically have non-physical negative values. The second-order time evolution algorithm presented here allows for more accurate solutions with larger time steps; however, it also can resolve the negativities that first-order time solutions smear out. Therefore, artificial scattering is studied to see how it can be used to decrease the oscillations in low-order solutions and prevent negativities. Small amounts of arbitrary, non-physical scattering can significantly improve the accuracy of the solution to test problems. Flux-limited diffusion solutions can also be improved by including artificial scattering. One- and two-dimensional test results are presented.

1. Introduction

In an earlier paper [1], a simple second-order time evolution method was demonstrated for the solution of the flux-limited diffusion approximation to the radiation transport equation. Those calculations included a material energy equation with thermal conduction. The algorithm was stable, robust, accurate, and computationally faster than the standard backward Euler first-order solution. Here that algorithm will be shown to be equally effective for the time evolution of the P_N representation of the transport equation.

Because of the great computational cost of high angular-order solutions of the transport equation, low-order approximations are of great interest and there exist a great variety of different approximations (see [2]). If the angular variables are replaced by polynomials, one has P_N or spherical harmonics methods. If the angles are sampled at specific angles with given weights, then one generically has S_N or discrete ordinates methods. For large N, both approaches can give accurate representations of the transport equation. At low order, both methods have problems. Discrete ordinates methods suffer from what are called "ray effects". This problem has been studied for decades and has an extensive literature. See this textbook [3] and a recent paper [4] for examples and earlier references.

All orders of the P_N approximation have continuous representations in angle and therefore do not suffer from ray effects. Instead they display space–time oscillations that are just as onerous as ray effects and just as difficult to deal with in numerical algorithms, especially at low order where the amplitudes of the oscillations are larger. In some problems the oscillations are large enough to drive the radiation energy negative. The inherent positivity properties of the P_N and the simplified P_N methods are discussed in [5]. They derive a simplified P_3 that is strictly positive, but it is probably too diffusive and too specialized to be useful in practical calculations. More discussion of P_N positivity is given in [9]. There are ways to reduce spatial

* Tel.: +1 608 836 1779.
E-mail address: olson99@tds.net

0021-9991/$ - see front matter © 2009 Elsevier Inc. All rights reserved.
doi:10.1016/j.jcp.2009.01.012

oscillations by using a Riemann solver and upwind discretization or discontinuous Galerkin methods [6–11]. Unfortunately, some of these methods give results that do not match the asymptotic diffusion limit and would not be acceptable for most thermal radiation transport problems. Most of these more sophisticated spatial discretizations add significantly to the nonlinearity of the equations and are still in the research stages of their development. Some of them exist only on 1D meshes. Therefore, the spatial discretization presented in Section 2 is a simple one that conserves energy locally and reduces to central differencing when opacities are constant.

In Ref. [2], the lowest-order expansion, linear in angle, P_1 representation was modified so that it had the correct propagation velocity in optically thin media. The unmodified equation causes wave fronts to propagate at $c/\sqrt{3} \approx 0.577c$ instead of c, where c is the speed of light. The improved P_1 was obtained simply by multiplying the time derivative term in the flux equation by a scale factor (see the next section). This modification to the P_1 equation does not affect its diffusion limit [12], but it does affect the time scale for the damping of transient waves [13]. Similar modifications will be shown for $N = 3$ and 5 in Section 3 of this paper. In addition to correcting the propagation velocity in thin media, these modifications decrease the amplitude of the oscillations in the numerical solutions. Unfortunately, this decrease does not eliminate the problem of negative radiation energy density; it just decreases the severity of the problem slightly.

The problem with low-order methods is that the radiation gets lumped into a small number of angles or a low-order polynomial that poorly represent reality. The scattering of photons is a physical process that redistributes the photons from one angular direction to another. Here, artificial scattering will be used as a numerical adjustment to smear out the solution from low-order P_N to better approximate the correct solutions to some test problems. It will be shown in Sections 4 and 5 that small amounts of scattering can also improve the accuracy of flux-limited diffusion solutions.

The next section of this paper will derive the equations for the second-order time evolution of the P_1 equations. Then a slightly different algorithm will be shown for $N = 3$ and 5 in Section 3. These methods will be compared to Su and Olson [14] and McClarren et al. [15] analytic test problem in Section 4. Following in Section 5 will be a comparison to an optically thin test problem. A two-dimensional, multi-material problem will be presented in Section 6. A brief summary is in Section 7.

2. P_1 equations

Following the notation used in earlier work [1,2], the zeroth- and first-angular moments of the transport equation are written as:

$$\frac{1}{c}\frac{\partial E}{\partial t} + \nabla \cdot F = \sigma_a(T^4 - E), \tag{1}$$

$$\frac{\eta}{c}\frac{\partial F}{\partial t} + \frac{1}{3}\nabla E = -\sigma_t F. \tag{2}$$

Here E is the radiation energy density, t is time, c is the speed of light, F is the radiation flux, σ_a is the absorption opacity, T is the material temperature, η is an adjustable coefficient, and σ_t is the total opacity, the sum of absorption and scattering ($\sigma_t = \sigma_a + \sigma_s$). Here we are using units such that $E = T_r^4$, where T_r is the radiation temperature. The adjustable coefficient, η, is set to unity for the standard P_1 equation. To have a wave front in a thin medium propagate at c, η must be set to a value of 1/3. Results will be shown for the full range of η. The diffusion approximation is achieved by setting $\eta = 0$. The material equation to be solved with the above radiation moment equations is given by:

$$\frac{c_V}{c}\frac{\partial T}{\partial t} - \nabla \cdot (K\nabla T) = \sigma_a(E - T^4), \tag{3}$$

where c_V is the heat capacity, and K is the material conduction coefficient.

The time evolution of these equations will use a three-time level backward difference formula that reference [1] generalized to variable time steps:

$$E^{n+1} = aE^n + (1-a)E^{n-1} + b\Delta t\left.\frac{\partial E}{\partial t}\right|^{n+1}, \tag{4a}$$

$$a = \frac{(1+\rho)^2}{1+2\rho}, \quad b = \frac{1+\rho}{1+2\rho}, \quad \rho = \frac{t^{n+1} - t^n}{t^n - t^{n-1}}, \tag{4b}$$

where Δt is the time step, $\Delta t = t^{n+1} - t^n$, and n indicates the time level. In practical calculations, one limits how quickly the time step is allowed to increase so that $0.1 \leqslant \rho \leqslant 1.25$. Therefore, the coefficients in Eq. (4) are very well behaved. For constant time step size, ρ is unity, $a = 4/3$, and $b = 2/3$. Ref. [10] used the constant time step version for solving the radiation only P_N equations. Ref. [1] showed that this numerical scheme is robust over a wide range of time steps when solving flux-limited diffusion coupled to material conduction. Here that same robustness will be shown for solving the P_1 equations with and without material conduction. Inserting Eq. (1) into (4) and rearranging the terms gives

$$(1 + bc\Delta t\sigma_a^{n+1})E^{n+1} + bc\Delta t\nabla \cdot F^{n+1} = aE^n + (1-a)E^{n-1} + bc\Delta t\sigma_a^{n+1}(T^{n+1})^4. \tag{5}$$

Similarly, using the form of Eq. (4) for the radiation flux and material temperature and inserting Eqs. (2) and (3) produces

$$(1 + bc\Delta t\sigma_t^{n+1}/\eta)F^{n+1} + \frac{bc\Delta t}{3\eta}\nabla E^{n+1} = aF^n + (1-a)F^{n-1} \tag{6}$$

and

$$\left[1 + \frac{bc\Delta t\sigma_a^{n+1}}{c_V^{n+1}}(T^{n+1})^3\right]T^{n+1} - \frac{bc\Delta t}{c_V^{n+1}}\nabla\cdot(K^{n+1}\nabla T^{n+1}) = aT^n + (1-a)T^{n-1} + \frac{bc\Delta t\sigma_a^{n+1}}{c_V^{n+1}}E^{n+1}. \tag{7}$$

The energy balance equation, Eq. (5), is strongly coupled to the material equation, Eq. (7), through the absorption and emission terms. All three equations are strongly nonlinear because of the implicit evaluation of the opacities, heat capacity, and thermal conduction coefficient. Ref. [1] showed that a linearization of the material temperature and a simple operator splitting technique can be used to efficiently solve the flux-limited diffusion version of these equations. Since the temperature and material coupling terms here are identical to the flux-limited diffusion equations, that same linearization and operator splitting works well with these equations. Readers interested in a more detailed discussion should read [1]. Only an outline of the full derivation and explanation is presented here.

The nonlinearity of the temperature can be removed by using a Taylor series expansion:

$$(T^{n+1})^4 \approx (T^*)^4 + \Delta T\frac{\partial (T^*)^4}{\partial T} = (T^*)^4 + (T^{n+1} - T^*)4(T^*)^3 = (T^*)^3(4T^{n+1} - 3T^*), \tag{8}$$

where T^* is a reference temperature. In order to get second-order accuracy, one should use the previous iteration's value of $T^{n+1}$for T^*. As the iterations at each time step converge, the equation coefficients and the physical variables $(\sigma_a^{n+1}, \sigma_t^{n+1}, c_V^{n+1}, K^{n+1})$ will be evaluated at the correct implicit temperature.

Solving Eq. (6) for F^{n+1} and substituting it into Eq. (5) results in two coupled diffusion-like equations for E^{n+1} and T^{n+1}. They could be solved simultaneously as one large system; however, Ref. [1] found that it was much more efficient computationally to use operator splitting to solve two smaller systems. The first phase of the operator split is to lag in time the conduction term in Eq. (7). Using Eq. (8), one can then solve for the temperature

$$\left[1 + \frac{4bc\Delta t\sigma_a^{n+1}}{c_V^{n+1}}(T^*)^3\right]T' = aT^n + (1-a)T^{n-1} + \frac{bc\Delta t\sigma_a^{n+1}}{c_V^{n+1}}[E' + 3(T^*)^4] + \frac{bc\Delta t}{c_V^n}\nabla\cdot(K^n\nabla T^n), \tag{9}$$

where the prime superscript designates an intermediate time between n and $n+1$. Inserting this result into Eq. (5) and rearranging the terms gives

$$\begin{aligned}&\left[1 + \frac{bc\Delta t\sigma_a^{n+1}}{1 + \frac{4bc\Delta t\sigma_a^{n+1}}{c_V^{n+1}}(T^*)^3}\right]E' - bc\Delta t\nabla\cdot F' \\ &\quad = aE^n + (1-a)E^{n-1} + \frac{4bc\Delta t\sigma_a^{n+1}(T^*)^3}{1 + \frac{4bc\Delta t\sigma_a^{n+1}}{c_V^{n+1}}(T^*)^3}\left[aT^n + (1-a)T^{n-1} - \frac{3}{4}T^* + \frac{bc\Delta t}{c_V^n}\nabla\cdot(K^n\nabla T^n)\right],\end{aligned} \tag{10}$$

where, for simplicity of notation, the flux from Eq. (6) has not been inserted. Eq. (10) is a diffusion-like equation with a more complicated than usual main diagonal and right hand side. In one dimension, it represents a tridiagonal system of equations, while in 2D there are five diagonals. Once Eq. (10) is solved for the time advanced radiation energy density, Eq. (9) is trivial to solve for the new material temperature.

The second phase of the operator split is to solve for the implicit nonlocal material conduction and update the radiation energy density for the new temperature through the local absorption and emission. After some intermediate steps shown in [1], one obtains

$$\begin{aligned}&\left[1 + \frac{4bc\Delta t\sigma_a^{n+1}(T^*)^3}{(1 + bc\Delta t\sigma_a^{n+1})c_V^{n+1}}\right]T^{n+1} - \frac{bc\Delta t}{c_V^{n+1}}\nabla\cdot(K^{n+1}\nabla T^{n+1}) \\ &\quad = T' + \frac{bc\Delta t\sigma_a^{n+1}}{(1 + bc\Delta t\sigma_a^{n+1})c_V^{n+1}}[(T')^4 + 3(T^*)^4] - \frac{bc\Delta t}{c_V^n}\nabla\cdot(K^n\nabla T^n),\end{aligned} \tag{11}$$

$$E^{n+1} = E' + bc\Delta t\sigma_a^{n+1}[(T^{n+1})^4 - (T')^4]/(1 + bc\Delta t\sigma_a^{n+1}). \tag{12}$$

After a diffusion solve for the temperature, the update to the energy density is easy. With a new temperature, the physical coefficients must be reevaluated and the process repeated until convergence is achieved. However, it was found in [1,16] that incomplete convergence of this type of iteration does not destroy second-order accuracy. Most numerical cells converge immediately to their final result. Only cells near wave fronts and gradients are slower to converge. Stopping at three iterations did not cause any accumulation of errors in the test problem studied in [1]. That same multi-material problem is used in Section 6 to test the P_1 equations and the same result is found. Therefore, all the 2D calculations shown here will use a maximum of three iterations per time step.

Since the radiation momentum equation, Eq. (6), is quite different from the flux-limited diffusion equation analyzed in [1], some additional discussion needs to be given as to how it is finite differenced. This is most easily presented in one dimension. The generalization to multi-dimensions is straightforward. Traditionally, a staggered mesh is used where the radiation energy density is located at cell centers and the flux is on cell edges. Quantities that are at cell centers are labeled with a subscript of i, while $i \pm 1/2$ is used for cell edges. The opacities are assumed to be constant within a cell and the energy density is represented as piecewise linear within each half of a cell, from cell center to cell face. The 1D flux from Eq. (6) can be evaluated as two different expressions, one from the right and one from the left cell. However, since E and F are assumed to be continuous at a cell face, these two finite differences must be equal and give

$$\begin{aligned} F_{i+1/2}^{n+1} &= \beta_i^{n+1}\left[aF_{i+1/2}^{n} + (1-a)F_{i+1/2}^{n-1} - \frac{2bc\Delta t}{3\eta\Delta z}(E_{i+1/2}^{n+1} - E_i^{n+1})\right] \\ &= \beta_{i+1}^{n+1}\left[aF_{i+1/2}^{n} + (1-a)F_{i+1/2}^{n-1} - \frac{2bc\Delta t}{3\eta\Delta z}(E_{i+1}^{n+1} - E_{i+1/2}^{n+1})\right], \end{aligned} \tag{13}$$

where a temporary energy density has been introduced on the cell face, $E_{i+1/2}^{n+1}$, and the coefficient is defined as

$$\beta_i^{n+1} \equiv \frac{1}{1 + bc\Delta t\sigma_{t,i}^{n+1}/\eta}. \tag{14}$$

In order to keep the equations simpler, a uniform cell size of Δz is assumed. Solving for the face energy density gives

$$E_{i+1/2}^{n+1} = \frac{(\beta_i^{n+1} - \beta_{i+1}^{n+1})[aF_{i+1/2}^{n} + (1-a)F_{i+1/2}^{n-1}] + \frac{2bc\Delta t}{3\eta\Delta z}(\beta_i^{n+1}E_i^{n+1} + \beta_{i+1}^{n+1}E_{i+1}^{n+1})}{\frac{2bc\Delta t}{3\eta\Delta z}(\beta_i^{n+1} + \beta_{i+1}^{n+1})}. \tag{15}$$

Substituting this back into Eq. (13) gives

$$F_{i+1/2}^{n+1} = \beta_{i+1/2}^{n+1}\left[aF_{i+1/2}^{n} + (1-a)F_{i+1/2}^{n-1} - \frac{bc\Delta t}{3\eta\Delta z}(E_{i+1}^{n+1} - E_i^{n+1})\right], \tag{16}$$

where the coefficient averaged for the face is

$$\beta_{i+1/2}^{n+1} \equiv \frac{1}{1 + \frac{bc\Delta t}{2\eta}(\sigma_{t,i}^{n+1} + \sigma_{t,i+1}^{n+1})}. \tag{17}$$

Substituting Eq. (16) into Eq. (10) gives terms that look like traditional diffusion finite differencing and other terms from the flux at past time steps that are moved to the right hand side of the equation. By insisting that the flux is continuous across a cell face, this differencing scheme preserves energy locally. The energy that flows out of one cell face is identical to the energy that flows into the next one.

3. P_3 and P_5 equations

The next higher-order angular expansions will be presented here in only one dimension. The test problems analyzed with P_3 and P_5 will be one-dimensional slabs. Partially following Pomraning's [17] notation, the specific intensity of the radiation field, I, is expanded in terms of Legendre polynomials

$$I(z,\mu,t) = \sum_{l=0}^{\infty}\frac{(2l+1)c}{4\pi}\phi_l(z,t)P_l(\mu), \tag{18}$$

$$\phi_l(z,t) = \frac{2\pi}{c}\int_{-1}^{+1} d\mu P_l(\mu)I(z,\mu,t), \tag{19}$$

where l is the Legendre expansion order, μ is the angle cosine, z is the spatial coordinate, P_l is the lth Legendre polynomial, and ϕ_l is the lth Legendre moment of the radiation field. The one-dimensional transport equation can be written in the form

$$\frac{1}{c}\frac{\partial I}{\partial t} + \mu\frac{\partial I}{\partial z} - \sigma_a\left(\frac{cT^4}{4\pi} - I\right) - \sigma_s\left(\frac{cE}{4\pi} - I\right) = 0. \tag{20}$$

Taking the zeroth angular moment of this transport equation produces

$$\frac{1}{c}\frac{\partial\phi_0}{\partial t} + \frac{\partial\phi_1}{\partial z} - \sigma_a(T^4 - \phi_0) = 0, \tag{21}$$

which is identical to Eq. (1) if one makes the identification $\phi_0 = E$ and $\phi_1 = F$. Higher Legendre moments of the transport equation can be written as

$$\frac{2l+1}{c}\frac{\partial\phi_l}{\partial t} + l\frac{\partial\phi_{l-1}}{\partial z} + (l+1)\frac{\partial\phi_{l+1}}{\partial z} - (2l+1)\sigma_t\phi_l = 0. \tag{22}$$

The traditional method for truncating this series expansion is to set $\phi_{l+1} = 0$. Therefore, for the P_3 expansion, in addition to Eq. (21), includes

$$\frac{\eta_1}{c}\frac{\partial\phi_1}{\partial t}+\frac{1}{3}\frac{\partial\phi_0}{\partial z}+\frac{2}{3}\frac{\partial\phi_2}{\partial z}-\sigma_t\phi_1=0, \tag{23}$$

$$\frac{\eta_2}{c}\frac{\partial\phi_2}{\partial t}+\frac{2}{5}\frac{\partial\phi_1}{\partial z}+\frac{3}{5}\frac{\partial\phi_3}{\partial z}-\sigma_t\phi_2=0, \tag{24}$$

$$\frac{\eta_3}{c}\frac{\partial\phi_3}{\partial t}+\frac{3}{7}\frac{\partial\phi_2}{\partial z}-\sigma_t\phi_3=0, \tag{25}$$

where the factors on the time derivatives are introduced just as in Eq. (2). The material equation using the notation in this section becomes

$$\frac{c_V}{c}\frac{\partial T}{\partial t}-\nabla\cdot(K\nabla T)-\sigma_a(\phi_0-T^4)=0. \tag{26}$$

Using the form of the time evolution in Eq. (4) for each of the P_3 equations and rearranging the terms yields

$$[1+bc\Delta t\sigma_{a,i}^{n+1}]\phi_{0,i}^{n+1}=a\phi_{0,i}^{n}+(1-a)\phi_{0,i}^{n-1}-bc\Delta t\left[\frac{1}{\Delta z}(\phi_{1,i+1/2}^{n+1}-\phi_{1,i-1/2}^{n+1})-\sigma_{a,i}^{n+1}(T_i^{n+1})^4\right], \tag{27}$$

$$\left[1+\frac{bc\Delta t}{2\eta_1}(\sigma_{t,i}^{n+1}+\sigma_{t,i+1}^{n+1})\right]\phi_{1,i+1/2}^{n+1}=a\phi_{1,i+1/2}^{n}+(1-a)\phi_{1,i+1/2}^{n-1}-\frac{bc\Delta t}{3\eta_1\Delta z}[\phi_{0,i+1}^{n+1}-\phi_{0,i}^{n+1}+2(\phi_{2,i+1}^{n+1}-\phi_{2,i}^{n+1})], \tag{28}$$

$$\left[1+\frac{bc\Delta t}{\eta_2}\sigma_{t,i}^{n+1}\right]\phi_{2,i}^{n+1}=a\phi_{2,i}^{n}+(1-a)\phi_{2,i}^{n-1}-\frac{bc\Delta t}{5\eta_2\Delta z}[2(\phi_{1,i+1/2}^{n+1}-\phi_{1,i-1/2}^{n+1})+3(\phi_{3,i+1/2}^{n+1}-\phi_{3,i-1/2}^{n+1})], \tag{29}$$

$$\left[1+\frac{bc\Delta t}{2\eta_3}(\sigma_{t,i}^{n+1}+\sigma_{t,i+1}^{n+1})\right]\phi_{3,i+1/2}^{n+1}=a\phi_{3,i+1/2}^{n}+(1-a)\phi_{3,i+1/2}^{n-1}-\frac{3bc\Delta t}{7\eta_3\Delta z}(\phi_{2,i+1}^{n+1}-\phi_{2,i}^{n+1}), \tag{30}$$

$$\left[1+\frac{4bc\Delta t\sigma_{a,i}^{n+1}}{c_{V,i}^{n+1}(T_i^*)^3}\right]T_i^{n+1}=aT_i^{n}+(1-a)T_i^{n-1}+\frac{bc\Delta t\sigma_{a,i}^{n+1}}{c_{V,i}^{n+1}}[\phi_{0,i}^{n+1}+3(T_i^*)^4]. \tag{31}$$

The material conduction term has been dropped from Eq. (31) because the 1D test problems presented in the next two sections do not include that physics. In Eqs. (28) and (30), note that the total opacity has been averaged just as was done in Eq. (17).

Because of the spatial derivative of ϕ_2 in Eq. (23), it is not possible to follow the P_1 procedure from the previous section of combining the zeroth and first moment equations to obtain a single equation for the radiation energy density. Since the purpose of this paper is only to evaluate test problems in one dimension and not to build a robust 1D algorithm, Eqs. (27)–(31) will be used as presented. More iterations are required than if a more sophisticated algorithm were used; however, as long as the time step is kept small, the iteration process converges quickly. In Section 5, a simple test problem will demonstrate a lack of convergence for large time steps.

For the P_5 equations, one replaces Eq. (30) and adds two equations for the next higher moments

$$\left[1+\frac{bc\Delta t}{2\eta_3}(\sigma_{t,i}^{n+1}+\sigma_{t,i+1}^{n+1})\right]\phi_{3,i+1/2}^{n+1}=a\phi_{3,i+1/2}^{n}+(1-a)\phi_{3,i+1/2}^{n-1}-\frac{bc\Delta t}{7\eta_3\Delta z}[3(\phi_{2,i+1}^{n+1}-\phi_{2,i}^{n+1})+4(\phi_{4,i+1}^{n+1}-\phi_{4,i}^{n+1})], \tag{32}$$

$$\left[1+\frac{bc\Delta t}{\eta_4}\sigma_{t,i}^{n+1}\right]\phi_{4,i}^{n+1}=a\phi_{4,i}^{n}+(1-a)\phi_{4,i}^{n-1}-\frac{bc\Delta t}{9\eta_4\Delta z}[4(\phi_{3,i+1/2}^{n+1}-\phi_{3,i-1/2}^{n+1})+5(\phi_{5,i+1/2}^{n+1}-\phi_{5,i-1/2}^{n+1})], \tag{33}$$

$$\left[1+\frac{bc\Delta t}{2\eta_5}(\sigma_{t,i}^{n+1}+\sigma_{t,i+1}^{n+1})\right]\phi_{5,i+1/2}^{n+1}=a\phi_{5,i+1/2}^{n}+(1-a)\phi_{5,i+1/2}^{n-1}-\frac{5bc\Delta t}{11\eta_5\Delta z}(\phi_{4,i+1}^{n+1}-\phi_{4,i}^{n+1}). \tag{34}$$

The material equation is not changed.

Marshak boundary conditions are applied to the odd moments at the left and right boundaries. For isotropic incident radiation fields at $z = 0$ and $z = Z$,

$$I(0,\mu,t)=\frac{cI^{inc}(0,t)}{4\pi}\quad\text{for }\mu\geqslant 0, \tag{35a}$$

$$I(Z,\mu,t)=\frac{cI^{inc}(Z,t)}{4\pi}\quad\text{for }\mu\leqslant 0, \tag{35b}$$

the odd Legendre moments on the boundary are

$$\phi_1^{inc}(0,t)=\frac{1}{4}I^{inc}(0,t),\quad \phi_3^{inc}(0,t)=-\frac{1}{16}I^{inc}(0,t),\quad \phi_5^{inc}(0,t)=\frac{1}{32}I^{inc}(0,t), \tag{36a}$$

$$\phi_1^{inc}(Z,t)=-\frac{1}{4}I^{inc}(Z,t),\quad \phi_3^{inc}(Z,t)=\frac{1}{16}I^{inc}(Z,t),\quad \phi_5^{inc}(Z,t)=-\frac{1}{32}I^{inc}(Z,t). \tag{36b}$$

For the test problems in Sections 4 and 6, reflecting boundary conditions are required. Then the odd Legendre moments on the boundaries are fixed at zero.

Before solving these equations, the scale factors on the time derivatives, the η's, must be specified. For the P_1 equations a simple analysis shows that $\eta = 1/3$ is required to achieve wave propagation at the correct value of c in low opacity media. For the higher-order methods, the correct coefficients are determined here from numerical experiments. For P_3 and P_5, there are, respectively, three and five different coefficients with many different values possible. After examining many options, three choices seemed to be the most appropriate. (a) Modify only the coefficient in the highest-order equation, leaving the others at unity. (b) Modify only the odd moment coefficients, setting them equal to each other, and leave the even-order coefficients at unity. (c) Modify all coefficients equally, setting them all to the same value. Table 1 shows the resulting coefficients that give a propagation velocity of c.

Calculations done with each set of η parameters are similar, but not identical, to calculations done with the other sets. The shape of the wave being propagated is slightly different in each case. In principle, one could adjust the coefficients to give a best fit to a particular problem of interest. However, there is no guarantee that such a choice of coefficients would also be best for the next problem.

Ref. [9] made the suggestion of using a diffusion-like approximation for the highest P_N order by dropping the time derivative term. Presumably, this approximation would decrease the oscillations in the numerical solutions, but it also significantly increases the wave propagation velocity. For P_5, decreasing η_5 from 0.44 to 0.2 increases the wave speed from c to $1.24c$. This seems to be an unacceptably large increase. Therefore, this author attempted to use some flux-limited diffusion-like approximations for Eq. (34). Numerical difficulties arose that prevented successful calculations; therefore, this approach was discontinued.

4. One-dimensional Su and Olson test problem

An analytic solution to the transport equation coupled to a material equation without conduction has been published in [14] that corresponds to using $N = \infty$. In order to make the solution tractable, the opacity was chosen to be constant ($\sigma_a = 1$) and the heat capacity was chosen to be proportional to the cube of the material temperature. This enables a transformation that converts the material equation into a form that is linear in T^4. An internal source of radiation is used along with reflecting boundary conditions. See [14] for a complete description and [2] for comparisons of other approximate solutions to this analytic solution. More recently, an analytic solution for the P_1 approximation to this test problem has been published [15]. This allows one to directly test the solution of the lowest-order equations given by Eqs. (1) and (2). As the spatial and temporal meshes are refined, the numerical solution must converge to the analytic solution. The numerical solutions presented here do converge to the analytic solution. While the analytic solutions use an initial condition of zero radiation energy density, for convenience, the numerical solutions here use a finite initial radiation energy density of 10^{-4}.

Unfortunately, the analytic solutions in [14,15] are tabulated on spatial meshes that are too coarse to be used to demonstrate second-order temporal convergence. Therefore, a numerical solution using a very small time step will be used as a reference solution. Define the time step tolerance for change as

$$\tau = \max\left[\max_i\left(\frac{2(E_i^{n+1}-E_i^n)}{E_i^{n+1}+E_i^n}\right), \max_i\left(\frac{2(T_i^{n+1}-T_i^n)}{T_i^{n+1}+T_i^n}\right)\right], \tag{37}$$

where the maximum over i represents all cells. Based on the changes between two times, the next time step, Δt, is chosen to give the desired value for τ. The accuracy of the numerical solution will be shown for the range $0.0125 \leqslant \tau \leqslant 1.25$. As a convergence metric, the root mean square relative difference of the radiation energy density from the reference solution is defined as

$$\text{RMS Error} \equiv \sqrt{\frac{4}{N}\sum_{i=1}^{N}\left[\frac{E_i - E_i^{ref}}{E_i + E_i^{ref}}\right]^2}. \tag{38}$$

The reference solution is done with $\tau = 0.00125$.

In Fig. 1, the P_1 solution uses $\eta = 1$ and is evolved to a time of $ct = 3$ on a spatial mesh of 300 points equally spaced from zero to 3. The first-order solutions are done with $a = b = 1$ in Eq. (4) and all the other time evolution equations. This choice gives a simple backward Euler solution. The first-order solution at $\tau = 0.1$ requires 632 time steps to reach $ct = 3$ while the

Table 1
Coefficients that give velocities of c.

	η_1	η_2	η_3	η_4	η_5
P_3	1.0	1.0	0.43		
P_3	0.74	1.0	0.74		
P_3	0.84	0.84	0.84		
P_5	1.0	1.0	1.0	1.0	0.44
P_5	0.87	1.0	0.87	1.0	0.87
P_5	0.924	0.924	0.924	0.924	0.924

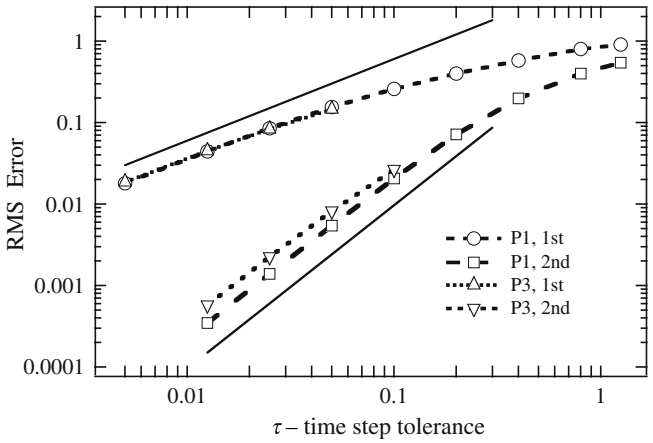

Fig. 1. The convergence error is shown as a function of the time step tolerance. The solid lines are for reference to show slopes of one and two.

second-order solution requires 831 time steps (31% more). The backward Euler solution required fewer time steps because it is more diffusive and smears out the solution at the front of the wave. At $\tau = 0.0125$, the backward Euler solution takes only 5% fewer time steps than the second-order method because there is much less numerical diffusion at this smaller time step.

The P_3 results shown in Fig. 1 use all η's = 1 and are done on a uniform mesh of 350 points from zero to 3.5. A slightly larger mesh is required than for P_1 because the wave front propagates faster with P_3. The errors are shown only for small time steps because the algorithm presented in the previous section does not converge for larger time steps. The algorithm is adequate for examining the oscillations in numerical solution, but it is not a robust general-purpose solution technique. The reference solution in this case is a P_3 solution done with the same small time step tolerance ($\tau = 0.00125$). There is no analytic solution for the $N = 3$ approximation.

Clearly, the second-order solutions in Fig. 1 are much more accurate than the first-order solutions. Over a wide range of time steps, the RMS Error closely follows the expected slope of two. The first-order solution shows linear convergence only for small time steps. When using even moderate-sized time steps, numerical diffusion spreads out the toe of the numerical solution. The RMS Error is chosen here to be a relative error; therefore, it is sensitive to errors at small values of the radiation energy density.

Now that second-order temporal convergence is demonstrated, the next step is to find ways to modify low angular-order solutions to look more like the high angular-order solution. Therefore, the computer code used by Su and Olson [14] was used to generate the exact solution to the full ($N = \infty$) transport solution on a much finer spatial mesh at a time of $ct = 3$ than was published in [14]. This allows one to use a least squares measure to determine the goodness of fits when trying to modify the low-order solutions to look like the high-order analytic solution. Because this problem has a source region that is one optical depth in size, and because the opacity is of the same order as the problem size, this problem is quite diffusive and it is easy to fit with moderate order of P_N. Also, because it includes absorption and re-emission by the material, there is already some effective scattering of photons. Therefore, there are no oscillations in any of the numerical solutions.

The best fit for a modified flux-limited diffusion solution was obtained using $\sigma_s = 0.25$. For the P_N solutions there are two approaches: (a) adjust the time scaling parameters (η's) using no artificial scattering, or (b) set the η's to give the correct wave propagation velocity and vary the artificial scattering to fit the problem. For P_1, good fits are found using (a) $\eta = 0.36$ and $\sigma_s = 0$, or (b) $\eta = 1/3$ and $\sigma_s = 0.26$. For P_3, the good fits are (a) $\eta_1 = \eta_2 = 1$, $\eta_3 = 0.52$, and $\sigma_s = 0$, or (b) $\eta_1 = \eta_2 = 1$, $\eta_3 = 0.43$, and $\sigma_s = 0.23$. For P_5, the two good fits use either (a) $\eta_1 = \eta_2 = \eta_3 = \eta_4 = 1$, $\eta_5 = 0.65$, and $\sigma_s = 0$, or (b) $\eta_1 = \eta_2 = \eta_3 = \eta_4 = 1$, $\eta_5 = 0.44$, and $\sigma_s = 0.11$. This problem is so easy that a slightly modified P_5 solution almost exactly goes through the analytic solution. No figures of these solutions are shown here because the curves differ so little from each other that a meaningful graphical representation is difficult to create. Refs. [2,14,15] present graphs of the solutions to these problems for the reader interested in visual representations.

Only mild conclusions can be reached from this test problem. Small amounts of artificial scattering improve the accuracy of flux-limited diffusion and low-order P_N solutions. Only a moderate order is required to accurately reproduce this analytic solution.

5. One-dimensional optically thin test problem

To test transport in an optically thin medium, the absorption opacity is fixed at 0.1 with no temperature dependence. Isotropic radiation with unit intensity is applied to the left boundary and zero intensity is applied to the right side. Initially, the slab has zero radiation energy density. In order to make this a simple radiation only problem, the material temperature is set to zero and no material equation is solved. The exact full transport solution to this problem can be found in terms of expo-

nential integrals, but the details are not relevant here. For a small opacity, the distribution of radiation energy density in space looks roughly like a triangle with its base expanding at the speed of light.

Fig. 2 shows the P_1 numerical solution to this problem at a time of $ct = 3$. The analytic solution to the P_1 equations in this case is given by

$$E = \frac{1}{2}\exp\left(-\frac{\sigma x\sqrt{3\eta}}{ct}\right) \quad \text{for } x < \frac{ct}{\sqrt{3\eta}}. \tag{39}$$

For larger values of x the energy density is zero. So the exact solution has a gradual monotonic decrease from 0.5 at the origin until it gets to the wave front and then it drops discontinuously to zero. This discontinuity causes the numerical oscillations seen in Fig. 2. Using the same time step size, a backward Euler solution has smaller oscillations. However, as the time step is decreased, the oscillations in a first-order solution grow to match the oscillations of the second-order solution. When η is decreased from unity to 1/3, the wave propagates farther in the same amount of time so the discontinuity at the wave front is smaller. This causes the amplitude of the numerical oscillations to be smaller. The discontinuity is the result of truncating the transport solution by assuming a linear variation in angle. The oscillations are the result of the spatial discretization's approximation to the discontinuity.

Arbitrarily adding scattering to the solution makes a dramatic change, as shown in Fig. 2. The oscillations are reduced to tiny wiggles and the over all shape more closely follows the full transport analytic solution. Physically, artificial scattering is redistributing the photons away from the assumed linear distribution, thus greatly reducing the spatial discontinuity. This problem with streaming radiation is being made to look more diffusive.

Ref. [1] found that simple time-centered Crank–Nicolson second-order time differencing generated non-physical numerical oscillations when using large time steps in the solution of the diffusion equation for the 2D test problem discussed in the next section. The oscillations shown in Fig. 2 are of a quite different nature. As the time steps are increased, the oscillations smear out in space because numerical diffusion increases. They do not get worse with large time steps. As mention in the Introduction, different spatial discretizations will generate different sized oscillations. Therefore, the results presented here are specific to the spatial and temporal differencing presented in Section 2. This author has not seen any cases of numerical oscillations caused by the second-order time evolution scheme used here; however, McClarren et al. [10] refer to unpublished calculations where this scheme may have caused unexpected oscillations.

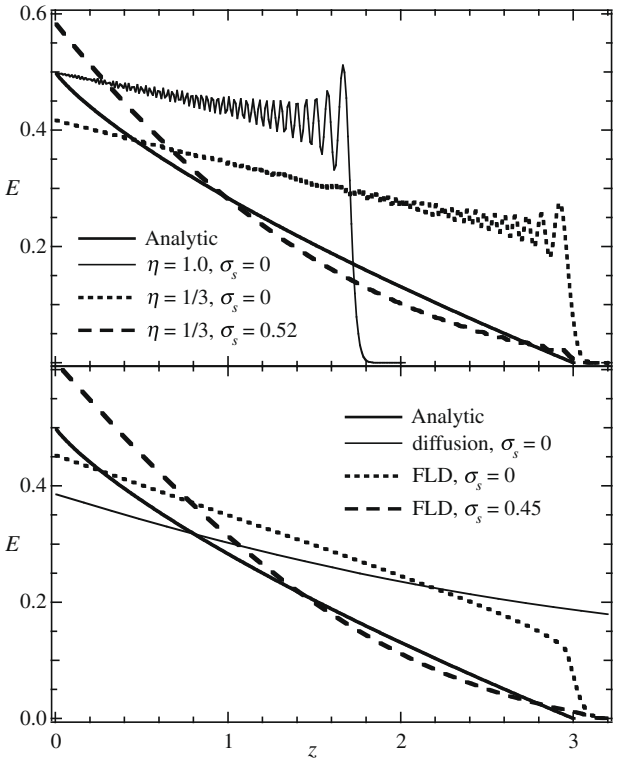

Fig. 2. The upper half compares three P_1 numerical solutions to the thin test problem at $ct = 3$ to the full transport analytic solution. The lower half compares diffusion and flux-limited diffusion (FLD) solutions.

Ref. [18] proposes a hybrid backward Euler and Crank–Nicolson scheme to reduce oscillations induced by time discretization. Their method uses the numerical diffusion of the first-order method to smear out oscillations. Using an artificial scattering opacity alters the differential equation to reduce the discontinuities and numerical oscillations caused by either time or spatial discretizations. The advantages and disadvantages of these two different approaches depend on personal preferences and the particular problem being solved. In the next section, it will be shown that artificial scattering can also be used to reduce P_N wave oscillations that are not caused by numerical discretizations.

Fig. 2 also shows diffusion solutions with and without flux limiting. With no flux limiting the radiation flows quickly out of the shown solution domain and far too much energy is propagated into the slab. Adding a flux limiter (see discussions in [1,2]) limits how far the radiation penetrates. One inherent feature of diffusion is that there are no oscillations, but this gain is at the expense of adding a nonlinearity to the equations through the flux limiter. Like P_1, diffusion assumes that the radiation intensity varies linearly in angle. Therefore, too much energy is propagated too quickly and the solution is greatly improved by adding some artificial scattering.

Fig. 3 shows the P_3 and P_5 solutions for this same thin slab problem. Comparing Figs. 2 and 3 shows that adding each odd order to the solution adds another level region and another discontinuity to the numerical solution. For the calculations in Fig. 3, only the highest order time coefficient was modified. The other scale factors were left at unity. The positions of each discontinuity in the solution can be modified by choosing different values for the η's. Artificial scattering was added in each case to provide a best fit in a least-squares sense to the analytic solution. Clearly, as the order of the approximation is increased, less artificial scattering is required. Increasing the propagation velocity to match the speed of light and including artificial scattering both decrease the oscillations in the solutions. However, the oscillations do not disappear. Adding enough artificial scattering to completely eliminate all oscillations causes the solutions to fall well below the full transport analytic solution. In an attempt to reduce the confusion of overlapping oscillating curves, the solution using $\eta_5 = 0.44$ and no artificial scattering is not shown. The unmodified P_5 solution propagates a wave front only a bit slow, at $0.94c$.

6. Two-dimensional multi-material test problem

An interesting and difficult 2D multi-material test problem that has a central blast wave moving out around two square objects was presented and used in [19,20]. The opacity varies inversely with the cube of the material temperature ($\sigma_a = 1/T^3$) and the square objects in the path of the radiation flow have opacities that are 1000 times larger than the surrounding medium. They [19,20] used a scaled hydrogen-like Saha ionization model for a simplified, but physically plausible heat capacity.

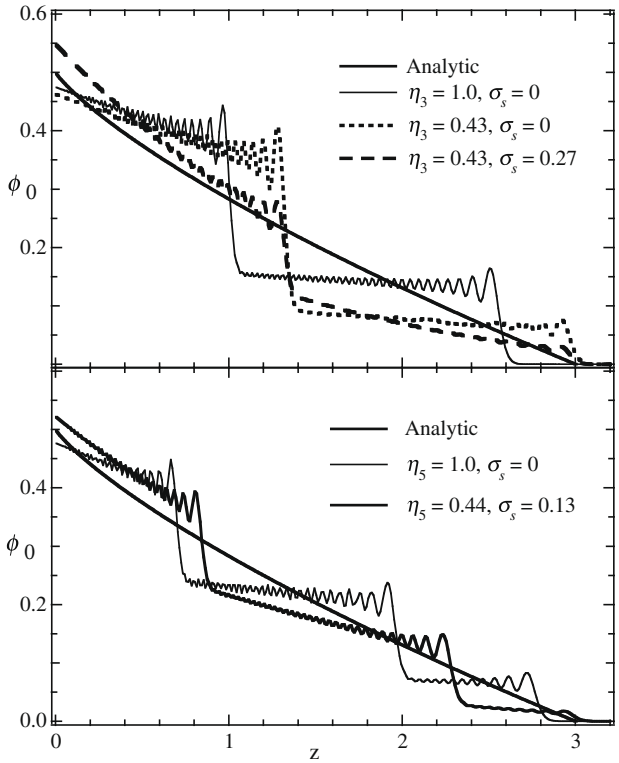

Fig. 3. The upper half compares P_3 solutions, while the lower half compares P_5 solutions to the optically thin slab test problem.

This added nonlinearity causes some numerical methods to fail when large time steps are used [21]. Here the mesh size will be 128^2 and the many details will be treated just as in [1]. The interested reader is referred to these earlier papers for more information.

Fig. 4 shows the time evolution for a P_1 solution (with $\eta = 1/3$) of the radiation energy density along one axis of this test problem. The radiation is initially peaked with a Gaussian shape centered at the origin and the material temperature is set equal to the radiation temperature: $T = T_r = E^{0.25}$. The maximum energy density at the origin is 100 while the minimum away from origin is 10^{-3}; therefore, the minimum temperature is $T = 10^{-0.75} = 0.178$ and the maximum opacity in the main medium is $\sigma_a = 178$. The radiation flux is initially set to zero, $F(x,y,0) = 0$. The boundary conditions are reflective and there are no sources of energy. The flux-limited diffusion (FLD) solution does not develop the hole in the radiation energy density shown in Fig. 4. The negative values for E near the origin persist for many time steps. Because of its initial high temperature and the presence of thermal conduction, the material temperature does not go negative when using $\eta = 1/3$. However, if one uses $\eta = 1$, the radiation energy density is more negative and the material temperature does go negative. Because the Saha heat capacity is not defined for negative temperatures, this stops the calculation. Adding an artificial scattering of $\sigma_s = 3$ prevents E from going negative when using $\eta = 1/3$. For the case $\eta = 1$, an artificial scattering of 6 is required to prevent negative radiation energy densities.

The P_1 solution in this test problem is attempting to propagate the radiation as a ring that moves out from the origin. The artificial scattering is smearing this ring; therefore, the peak amplitude of the radiation energy density in this ring is decreased as the hole is filled. The ring is an artifact of this low-order solution and is inherent to the wave nature of the P_N equations. A full transport solution ($N = \infty$) would show the energy density decreasing monotonically from the center at all times. The added scattering is much smaller than the cold opacity; therefore, it has only a small effect on the outward propagation velocity. Because of the large opacities and the material coupling, there are no discontinuities or numerically induced oscillations in this test problem.

A P_5 solution would probably show three rings propagating out from the origin. Each ring would expand at a slightly different velocity. Until someone does the calculation, it is not known whether or not the energy density at the origin would become negative. If negativities occur, it is likely that a smaller artificial scattering would be required than for P_1.

The temporal convergence errors for this 2D problem are shown in Fig. 5. Both the P_1 and flux-limited diffusion solutions were done with an artificial scattering of 3. The P_1 solution used $\eta = 1/3$. Again, the first-order solutions were done with $a = b = 1$ in Eq. (4). Since the equations are being solved with the same time differencing and the same operator splitting, it is not surprising that the convergence errors for FLD and P_1 are essentially identical in Fig. 5. The results are shown at $ct = 6$, the same time used by other authors [1,19,20]. The first-order and second-order solutions closely follow the expected slopes.

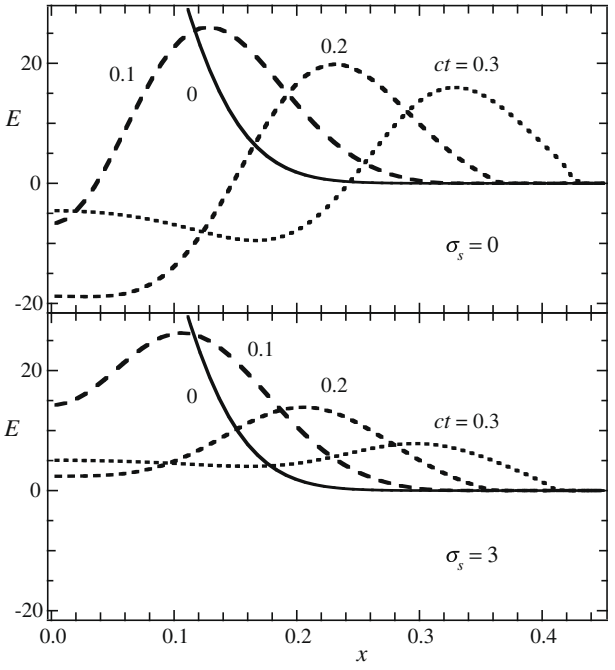

Fig. 4. P_1 solutions for the radiation energy density are shown along the x-axis at different times. The top panel has no artificial scattering while the bottom panel has added scattering as labeled.

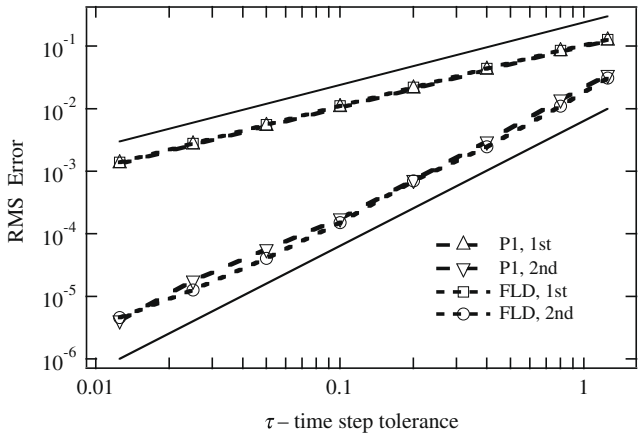

Fig. 5. Convergence error for the 2D test problem is shown as a function of the time step tolerance. The solid lines are for reference to show slopes of one and two.

As was found in [1], the second-order solutions take the same or slightly less computational time than the first-order solutions. For $\tau = 0.1$, the first-order solution used 1833 time steps and 385 s of computing time to get to $ct = 6$. The second-order solution used 1902 time steps and 374 s of computing time. The second-order method used 4% more time steps and 3% less computer time while generating a solution that has an RMS Error that is 60 times smaller. Most second-order methods take much more computational resources, time and memory, to achieve second-order time convergence. With the operator splitting technique used here and in [1], the only difference in the equations between first- and second-order are the values of the coefficients a and b. The second-order method does require an extra array of storage for the values at time level $n - 1$. When using the second-order technique, one has $b < 1$; therefore, the terms being iterated to convergence are smaller in second-order than in first-order. Therefore, the time required to reach convergence at each time step is slightly less in second-order. Slightly more time steps are used for the second-order solution because the wave front is slight steeper than when using the more diffusive backward Euler method. For more discussion of computational efficiency, see Ref. [1].

7. Summary

The second-order time evolution technique that Ref. [1] applied to the flux-limited diffusion equations has been applied here to the P_N equations. Second-order methods allow much larger time steps to be used. This is an advantage only if the second-order technique itself is not computationally expensive. Since the technique presented here and in [1] is computationally slightly faster and significantly more accurate than the first-order backward Euler method, it is a big improvement over first-order solutions.

Artificial scattering has been shown to dampen the oscillations in P_N solutions and can be used to prevent negative radiation energy densities. Including an artificial, non-physical scattering for numerical purposes is much easier than the different methods that have been used to reduce the problem of ray effects in low-order S_N solutions to the transport equation. It has been found that ray-effect mitigation techniques are highly problem dependent [4]. What works well for one problem with one geometry does not work well for the next problem with a different geometry. Adding artificial scattering will work much better in some problems than others. In radiation hydrodynamics problems with nonlinear opacities, a small amount of added scattering will have little effect on most of the solution. In neutron transport where scattering is a dominant part of the physics, adding scattering may distort the whole solution. The biggest advantage of artificial scattering is that it is numerically easy. One just increases the size of an existing term. No new numerical methods are required.

Also, it has been shown how simple scale factors on the time derivatives can be used to correct the velocity of wave propagation so that low-order P_N solutions exactly match the speed of light in optically thin media.

Acknowledgments

This author thanks an anonymous reviewer who pointed out the P_1 analytic solution, Eq. (39), to the test problem presented in Fig. 2. This reviewer also led to clarifications in the difference between numerical oscillations and P_N wave oscillations.

References

[1] G.L. Olson, Efficient solution of multi-dimensional flux-limited nonequilibrium radiation diffusion equation coupled to material conduction with second-order time discretization, J. Comput. Phys. 226 (2007) 1181–1195.

[2] G.L. Olson, L.H. Auer, M.L. Hall, Diffusion, P_1, and other approximate forms of radiation transport, JQSRT 64 (2000) 619–634.
[3] E.E. Lewis, W.F. Miller, Computational Methods of Neutron Transport, American Nuclear Society, Inc., La Grange Park, IL, USA, 1993.
[4] J.E. Morel, T.A. Wareing, R.B. Lowrie, D.K. Parsons, Analysis of ray-effect mitigation techniques, Nucl. Sci. Eng. 144 (2003) 1–22.
[5] M. Frank, A. Klar, E.W. Larsen, S. Yasuda, Time-dependent simplified P_N approximation to the equations of radiative transfer, J. Comput. Phys. 226 (2007) 2289–2305.
[6] R.B. Lowrie, J.E. Morel, Issues with high-resolution Godunov methods for radiation hydrodynamics, JQSRT 69 (2001) 475–489.
[7] R.G. McClarren, J.P. Holloway, Establishing an asymptotic diffusion limit for Riemann solvers on the time-dependent P_N equations, in: Mathematics and Computation, Supercomputing, Reactor Physics and Nuclear and Biological Applications, Avignon, France, September 2005, American Nuclear Society, LaGrange, 2005.
[8] R.G. McClarren, J.P. Holloway, A quasilinear implicit Riemann solver for the time-dependent P_N equations, Nucl. Sci. Eng. 155 (2007) 290–299.
[9] R.G. McClarren, J.P. Holloway, T.A. Brunner, On solutions to the P_N equations for thermal radiative transfer, J. Comput. Phys. 227 (2008) 2864–2885.
[10] R.G. McClarren, J.P. Holloway, T. Brunner, T. Mehlhorn, Implicit Riemann solvers for the P_N equations, in: F. Graziani (Ed.), Computational Methods in Transport, Granlibakken 2004, Springer-Verlag, 2006.
[11] R.G. McClarren, T.M. Evans, R.B. Lowrie, J.D. Densmore, Semi-implicit time integration for P_N thermal radiative transfer, J. Comput. Phys. 227 (2008) 7561–7586.
[12] J.E. Morel, Diffusion-limit asymptotics of the transport equation, the $P_{1/3}$ equations, and two flux-limited diffusion theories, JQSRT 65 (2000) 769–778.
[13] K.H. Simmons, D. Mihalas, A linearized analysis of the modified P_1 equations, JQSRT 66 (2000) 263–269.
[14] B. Su, G.L. Olson, An analytic benchmark for non-equilibrium radiative transfer in an isotropically scattering medium, Ann. Nucl. Eng. 24 (1997) 1035–1055.
[15] R.G. McClarren, J.P. Holloway, T.A. Brunner, Analytic P_1 solutions for time-dependent, thermal radiative transfer in several geometries, JQSRT 109 (2008) 389–403.
[16] R.B. Lowrie, A comparison of implicit time integration methods for nonlinear relaxation and diffusion, J. Comput. Phys. 196 (2004) 566–590.
[17] G.C. Pomraning, The Equations of Radiation Hydrodynamics, Pergamon Press, Oxford, 1973.
[18] R.G. McClarren, J.P. Holloway, A quasi-liner implementation of high-resolution time integration for the PN equations, Nucl. Sci. Eng. 159 (2008) 330–337.
[19] V.A. Mousseau, D.A. Knoll, New physics-based preconditioning of implicit methods for non-equilibrium radiation diffusion, J. Comput. Phys. 190 (2003) 42–51.
[20] V.A. Mousseau, D.A. Knoll, Temporal accuracy of the nonequilibrium radiation diffusion equations applied to two-dimensional multimaterial simulations, Nucl. Sci. Eng. 154 (2006) 174–189.
[21] R.M. Rauenzahn, V.A. Mousseau, D.A. Knoll, Temporal accuracy of the nonequilibrium radiation diffusion equations employing a Saha ionization model, Comput. Phys. Commun. 172 (2005) 109–119.